Electronic transitions induced by short-range structural order in amorphous TiO_2

C. A. Triana,[1,*] C. Moyses Araujo,[2] R. Ahuja,[2] G. A. Niklasson,[1] and T. Edvinsson[1]

[1]*Division of Solid State Physics, Department of Engineering Sciences, Ångström Laboratory, Uppsala University, Post Office Box 534, SE-751 21 Uppsala, Sweden*

[2]*Materials Theory Division, Department of Physics and Astronomy, Uppsala University, Post Office Box 516, S75120 Uppsala, Sweden*

(Received 10 May 2016; revised manuscript received 2 September 2016; published 14 October 2016)

Several promising applications of amorphous titanium dioxide, aTiO$_2$, have appeared recently, but the correlation between electronic properties and atomic short-range structural order is poorly understood. Herein we show that structural disorder yields local undercoordinated TiO_x units which influence electronic hybridization of Ti-[4p] and Ti-[3d] orbitals with a low crystal-field splitting [$E(e_g)$-$E(t_{2g}) = 2.4 \pm 0.3$ eV]. The short-range order and electronic properties of aTiO$_2$ thin-film oxides are described through an integrated approach based on x-ray-absorption experiments and *ab initio* computational simulations where the energy splitting of the electronic levels in the Ti-[4p-3d] manifold are analyzed. Structural disorder provides enough p-d orbital mixing for the hybridized electronic transitions from the Ti-[1s] core level into the [Ti-t_{2g}] and [Ti-e_g] bands [$1s \rightarrow 4p$-$3d$ excitations], to be allowed. This yields an intense pre-edge structure in the Ti K-edge x-ray-absorption near-edge structure spectrum of aTiO$_2$, which is consistent with the projected density of states on the photoabsorbing Ti atoms.

DOI: 10.1103/PhysRevB.94.165129

I. INTRODUCTION

Recently, amorphous titanium dioxide [aTiO$_2$] has gained increased attention due to its possibility for deposition at room temperature, which greatly simplifies deposition technologies. Thin-film oxides of aTiO$_2$ exhibit large roughness and porosity and hence a large surface area [1]. This simplifies diffusion of ionic species, making of aTiO$_2$ a promising electrode for applications in high-capability Li^+-Na^+-ion batteries [2,3], and electrochromic devices [4,5]. Particularly, aTiO$_2$ layers display potential applications in memristor switches [6], transistors [7], and anticorrosion coatings [8]. As stated by Anderson [9], Mott [10], and Cohen *et al.* [11], disorder generally induces localization of electronic states near the energy-gap edges. This yields band tails of occupied/unoccupied localized states, which extend into the mobility gap. Extended energy band tail states in disordered TiO_2 provide trapping sites for photoexcited charge carriers, avoiding their fast recombination, and providing effective electron-hole transfer, thus potentially increasing the photocatalytic efficiency [12]. In most nanoparticle systems, the surface is also less crystalline with surface reconstruction and disorder. Detailed knowledge of the atomic short-range structural order in amorphous transition-metal oxides [aTMOs] is thus necessary for understanding the electronic properties of not only fully amorphous systems but also of the vast class of nanoparticle systems investigated in a plethora of fields. It would thus be of great interest, and also crucial for the understanding of many systems to explain electronic properties as a function of structural disorder in aTiO$_2$.

In spite of attempts carried out to extract the atomic-structural order of aTiO$_2$ from experimental data, some results remain unclear. Previous studies on the pair distribution function [PDF] suggested that the local order of aTiO$_2$ resembles a brookitelike phase [13]. However, upon thermal heating, kinetics of phase transitions shows that aTiO$_2$ evolves into anatase or rutile rather than to a brookite phase [14]. Later studies on the PDF of aTiO$_2$ nanoparticles stated that such systems hold a distorted shell surrounding a crystalline anatase core [15]. However, studies of neutron diffraction [ND] and x-ray absorption [XAS] show that while such systems hold small amounts of crystalline anataselike domains, the mixture of several TiO_2 phases and undercoordinated TiO_x units must not be ruled out [16]. In fact, it has been shown that analysis based on PDF schemes is unreliable to recover the right statistic of two- and three-body correlations in the nearest atomic-coordination shells [17]. This yields underestimations in the distribution of Ti coordinations, which could explain why the reverse Monte Carlo [RMC] PDF modeled aTiO$_2$ nanoparticles exhibit XAS spectra that diverge from the measurements [15]. While those studies just assess the atomic local order, none of them analyze the electronic properties of the simulated amorphous systems. Band-structure calculations have shown that realization of tail states in aTiO$_2$ is due to dangling bonds created upon amorphization [18], and then electronic properties depend on the atomic local order generated by a specific amorphization scheme [19]. Thus, there is still need for a unified view of experimental data and theoretical models to correctly describe the dependence of the electronic properties on the atomic short-range order of aTiO$_2$. This unified approach is missing, and is valuable to understand band-tail states, electron localization, electron-hole transport, and polarons not only in aTiO$_2$ but also in other aTMOs.

In this work, we unify x-ray-absorption experiments with computational simulations to consistently describe the three-dimensional [3D] atomic short-range structural order and electronic properties of aTiO$_2$ thin-film oxides. Here, our main goal lies in studying the role of the local-range order on the electronic transitions giving rise to the x-ray-absorption near-edge structure [XANES] spectrum of aTiO$_2$. The atomic short-range structural order of aTiO$_2$ has been extracted by RMC simulations of the experimental extended x-ray-absorption fine-structure [EXAFS] spectra. RMC-EXAFS is a more advanced approach to analyze EXAFS spectra than standard EXAFS peak fitting. The last one employs small atomic clusters without periodic boundary conditions to optimize the relative weights of scattering paths, Debye-Waller factors σ^2, and ensemble parameters [17,20]. While standard EXAFS

*Corresponding author: Carlos.Triana@angstrom.uu.se

fitting merely provides average values of structural parameters, it does not have the ability to reproduce the full 3D structure of the system. Lack of single local order in amorphous systems yields a distribution of interatomic bond distances, bond angles, and ionic coordinations [21], that cannot be well resolved by standard EXAFS fitting. Studies of disordered systems based in Ti oxides usually deconvolute the pre-edge structure of XANES spectra in Gaussian and Lorentz functions, the peak heights, energy positions, and areas of which are compared against reference spectra of crystalline TiO_2 phases to estimate Ti coordination and population ratio [22–24]. This method provides qualitative information of atomic coordination, but it is only valid for few unequal Ti environments [25,26]. Moreover, its use is limited by the fact that normalized peak height versus energy position of pre-edge-XANES peaks depend not only on the ionic coordination but also on the static disorder in bond lengths, bond angles, experimental resolution, and formation of disordered domains arising from distinct deposition conditions [23,26]. The RMC-EXAFS approach applied here overcomes all those drawbacks. It provides statistical structural parameters along with fully optimized 3D structural models which fit the experimental EXAFS spectra and hold the right density of scattering centers. Inclusion of multiple scattering terms yields explicit treatment of three-body correlations [20]. Effects of static disorder due to fluctuations of interatomic bond distances, atomic coordinations, and bond angles are intrinsically taken into account by summing over large ensembles of atomic configurations, from which the structural ensemble-averaged EXAFS spectrum is computed.

Herein we show from RMC-EXAFS simulations a correct reproduction of the atomic short-range order of $a\text{TiO}_2$, matching its EXAFS-XANES spectra. Accuracy of structural models is analyzed by *ab initio* self-consistent real-space full multiple scattering [FMS] [27] and *ab initio* molecular dynamics [MD] simulations. Further, we go beyond structural analyses, and we unify the RMC-EXAFS simulated structures of $a\text{TiO}_2$ with finite difference methods [FDMs] [28], and hybrid density functional theory [DFT] [29], to assess correlations between local-range order and electronic properties. We analyze the electronic effects where disorder yields band-tail states, electronic hybridization, and *p-d* orbital mixing, which account for dipole hybridized electronic transitions from the Ti-[1*s*] core level into [Ti-t_{2g}; e_g] bands [$1s \rightarrow 4p - 3d$ excitations], in the pre-edge structure of the XANES spectra of $a\text{TiO}_2$. The unified approach presented here offers a systematic method to assess the short-range order of disordered materials and correlate it with the electronic properties.

II. EXPERIMENTAL METHODS

Thin-film oxides of $a\text{TiO}_2$ were deposited by reactive dc magnetron sputtering [thickness $\delta \approx 600 \pm 20$ nm, and density $\rho \approx 3.82\ \text{g/cm}^3$], with an O/Ti ratio of 2.00 ± 0.04 as determined by Rutherford backscattering spectrometry (RBS), and previously reported [4].

XANES and EXAFS at the Ti *K*-edge of $a\text{TiO}_2$ and reference anatase TiO_2 films were collected in fluorescence mode using a passivated implanted planar silicon (PIPS) detector, at beamline I811 at MAX-lab synchrotron source, Lund, Sweden [30]. The beam was focused employing a Si[111] double-crystal monochromator. Measured EXAFS spectra, $k^2\chi(k)$, were extracted by standard data reduction, absorption-edge energy calibration, and background subtraction, and then Fourier transformed to $\text{FT}|k^2\chi(k)|$ in the range $\Delta k = 2$–$10\ \text{Å}^{-1}$, as implemented in ATHENA [31]. Standard nonlinear least-squares EXAFS fitting was implemented to previously calculate interatomic distances, coordinations, and Debye-Waller factors σ^2. To this end, atomic clusters of $a\text{TiO}_2$ and anatase TiO_2 [space group $I41/\text{amdS}$; ICSD 9852], generated by ATOMS [31], were fitted to the experimental $k^2\chi(k)$ [in $\Delta k \approx 2$–$10\ \text{Å}^{-1}$], and $\text{FT}|k^2\chi(k)|$ [in $\Delta\text{R} \approx 0$–6 Å] spectra, using ARTEMIS [31]. Amplitudes and phase shifts for single- [Ti–O; Ti–Ti], and multiple-scattering [Ti–O–O; Ti–Ti–O; Ti–O–Ti–O] paths were self-consistently calculated using the *ab initio* real-space FMS FEFF8.4 code [27]. Fittings were done by allowing small fluctuations of interatomic bond distances and atomic coordinations. The σ^2 factors and the threshold energy shift ΔE_0 were used as free parameters.

III. COMPUTATIONAL SIMULATIONS

A. Reverse Monte Carlo RMC-EXAFS simulations

To simulate the local-structural order of $a\text{TiO}_2$, input structures comprising Ti=72 and O=144 atoms randomly distributed in cubic cells [$\text{V} \approx 2521\ \text{Å}^3$ and $\rho \approx 3.82\ \text{g/cm}^3$] were fitted to the experimental $k^2\chi(k)$ [in $\Delta k \approx 2$–$10\ \text{Å}^{-1}$] and $\text{FT}|k^2\chi(k)|$ [in $\Delta\text{R} \approx 0$–6 Å] spectra by RMC-EXAFS simulations as implemented in RMCProfile [32]. An amplitude reduction factor $S_0^2 \approx 0.94(2)$ was set from the overlapping integral in self-consistent calculations of the cluster potential by *ab initio* FMS in the muffin-tin approximation. The complex exchange correlation Hedin-Lundqvist self-energy potential and default values of the muffin-tin radii, as provided from FEFF8.4 [27], were used. Self-consistent calculations were implemented to have a more reliable determination of Fermi level, for accurate comparison with *ab initio* calculation of electronic structure. It also provides reliable EXAFS phase shifts and S_0^2 factors, considering the nonorthogonality of the initial- and final-state atomic orbitals of the absorbing atom. From preliminary EXAFS analysis by ARTEMIS, the threshold energy shift was set to $\Delta E_0 \approx -4.87$ eV. Amplitude and phase shifts for single- and multiple-scattering paths were calculated considering atoms up to $\text{R} \approx 7$ Å, from the photoabsorbing Ti atoms in the input atomic configurations. The following scattering paths between the absorbing Ti and scatterering ⊖;⊕=O;Ti atoms were used: (i) single scattering Ti⇄⊖; (ii) triple scattering Ti⇄⇄⊖; (iii) double and (iv) triple scattering in nearly collinear atomic chains with the absorber at the end of the chain Ti→⊖→⊕; Ti→⊖→⊖→⊕ [scattering angles ∢ = 0°–30°]; (v) double triangular scattering path with the absorber at the middle ⊖→Ti→⊕ [scattering angles ↗↘ = 10°–180°]; (vi) double scattering in triangular path with scatterers at first and second coordination shells around the absorber Ti→⊖→⊖ [scattering angles ↗; ∢ = 0°–40°]; and (vii) triple scattering in collinear chain with scatterers at the first coordination shell around the absorber, which by itself behaves as a scatterer ⊖→Ti→⊕ [scattering angles ↗↘ = 10°–180°]. Note

that although some single contributions arising from those multiple-scattering processes could be lower than others, their average contributions become important because there are a large number of them, and they vary among different amorphous structures of $a\text{TiO}_2$. Thermal damping of RMC-EXAFS signals associated to structural disorder σ^2 is given by the statistical average of $k^2\chi(k)^{\text{Ave}}_{\text{RMC}}$ spectra, calculated by summing over the ensemble of atomic configurations [17]. From preliminary EXAFS fitting by ARTEMIS, atoms were constrained to move into cutoff distances Ti–O $\approx$ 1.92–1.98 Å; O–O $\approx$ 2.56–2.74 Å; Ti–Ti $\approx$ 3.0–3.6 Å. This avoids the atoms getting too close and the breaking of Ti–O bonds. Average coordination constraints were inserted, and their weighting was gradually reduced at each RMC run. This led to average coordination distributions $N_{\text{Ti–O}} \approx 4.0$–$7.0$; $N_{\text{Ti-Ti}} \approx 2.0$–$3.0$, which were found to be the most suitable steady-state conditions to decrease the residual and reach spectral convergence. From a first RMC-EXAFS run, the structurally averaged $k^2\chi(k)_{\text{RMC}}$ [$\Delta k \approx 2$–10 Å^{-1}] spectra were calculated from all photoabsorbing Ti atoms in the input atomic configuration, and then Fourier transformed to $\text{FT}|k^2\chi(k)|_{\text{RMC}}$ [$\Delta\text{R} \approx 0$–6 Å]. The input atomic configurations were then optimized by allowing 3–5% of atoms to undergo displacements of $\approx$0.06 Å at each RMC cycle. Total $k^2\chi(k)_{\text{RMC}}$ and $\text{FT}|k^2\chi(k)|_{\text{RMC}}$ spectra equaling to the averaged single spectrum of each photoabsorbing Ti atom were recalculated every RMC cycle. Convergence to minimum residuals ~ 1–5×10^{-3} was attained by running ~ 6–8×10^5 RMC cycles. Eighteen structures of $a\text{TiO}_2$ unveiling similar short-range order were properly simulated and calculated structural correlation corresponds to the averaging over those RMC-EXAFS simulated structures.

B. Molecular-dynamics MD-EXAFS simulations

In order to validate our RMC-EXAFS implementation, and since RMC schemes lack a unique solution, *ab initio* MD simulations, as implemented in VASP [29], were carried out to extract "snapshots" of structural trajectories of $a\text{TiO}_2$, and compare them with those generated from RMC-EXAFS simulations. To this end, a cubic cell comprising Ti = 72 and O = 144 atoms [V $\approx$ 2521 Å^3, $\rho \approx 3.82$ g/cm^3], resized from the crystal symmetry of rutile TiO_2 [space group $P42/mnm$; ICSD 202241], was used as input structure. Amorphization was done by heating up to 5000 K [TiO_2 melting point $\approx$2116 K [19]]. MD was equilibrated in the liquid state for 2 ps, and then allowed to evolve for 2 ps, using 1-fs time steps at constant energy as a microcanonical ensemble. Then, thirty MD snapshots were selected and quenched down to 300 K, to simulate $a\text{TiO}_2$. Reaching of steady-state condition upon 10^4 ionic steps ensures that MD was energetically and structurally relaxed.

To assess the reliability of the MD snapshots of $a\text{TiO}_2$, MD-EXAFS functions $k^2\chi(k)_{\text{MD}}$ were computed by *ab initio* FMS and compared with measured $k^2\chi(k)$ spectra. The complex exchange-correlation Hedin-Lundqvist self-energy potential was used. The scattering potentials were computed in the muffin-tin approximation and muffin tins were overlapped to 1.15 to reduce effects due to potential discontinuities using FEFF8.4 [27]. $S_0^2 \approx 0.88(4)$ was estimated from the overlapping integral by self-consistent calculations of the cluster potential. Thermal damping of MD-EXAFS signals associated to the structural disorder, σ^2, is given by the statistical average of $k^2\chi(k)_{\text{MD}}$ spectra calculated by summing over the ensemble of thirty MD trajectories. Single Ti K-edge $k^2\chi(k)^{\text{Sin}}_{\text{MD}}$ functions were calculated for each absorbing Ti atom inside clusters of radii R = 7 Å, then averaged to a total $k^2\chi(k)_{\text{MD}}$ and Fourier transformed to a total $\text{FT}|k^2\chi(k)|_{\text{MD}}$ function.

C. *Ab initio* calculation of RMC- and MD-XANES

Ab initio calculations of the XANES spectra for both RMC-EXAFS and MD simulated structures of $a\text{TiO}_2$ were done in order to (i) validate the atomic coordination of photoabsorbing Ti atoms by reproduction of the pre-edge structure of the experimental XANES spectra and (ii) assess the electronic transitions $[t_{2g}; e_g]$ related to the electronic structure of unoccupied states in $a\text{TiO}_2$. The Ti K-edge RMC- and MD-XANES spectra were calculated self-consistently by *ab initio* FDM, as implemented in FDMNES [28]. Since FDM does not approximate the potential's form, it provides accurate descriptions on the structure of occupied/unoccupied electronic states. The real energy-dependent exchange Hedin-Lundqvist potential was used. The final excited state was approximated by relaxed configurations with a core hole at the [1s] level and an additional electron in the [4p] level for configurations Ti $\equiv$ [Ar]$3d^1 4s^2 4p^1$ and O $\equiv 1s^2 2s^2 2p^4$. Single Ti K-edge RMC- and MD-XANES spectra were calculated on a grid of 7 Å centered at each photoabsorbing Ti atom and averaged to total FDM-RMC and FDM-MD XANES spectra. FDM-XANES spectrum for anatase TiO_2 [space group I41/amdS; ICSD 9852], was calculated for comparison.

D. Hybrid density functional theory

Electronic properties of RMC-EXAFS simulated structures of $a\text{TiO}_2$ were studied by *ab initio* hybrid DFT [33], and used to describe the $1s \rightarrow 4p$-$3d$ dipole hybridized electronic transitions associated to the pre-edge structure of the XANES spectra of $a\text{TiO}_2$. Structural relaxation was done using the Perdew-Burke-Ernzerhof [PBE] functional [34], with the electron projector-augmented wave method [35], as implemented in VASP. A maximal force criterion convergence of 0.01 eV/Å was used, and an energy cutoff 400 eV was used to expand the Kohn-Sham orbitals in the plane-wave basis set. A $1 \times 1 \times 1$ Monkhorst-Pack mesh [36] at the Γ point was used for k sampling, and the nonlocal range separated screened hybrid functional HSE06 [20% HF; 80% PBE; $\omega = 0.2$ Å^{-1}] [37] was used.

IV. RESULTS AND DISCUSSION

A. Short-range order of $a\text{TiO}_2$ by RMC-EXAFS

Figure 1(a) shows spectral fitting from RMC-EXAFS simulations $k^2\chi(k)_{\text{RMC}}$ to the experimental $k^2\chi(k)$ spectrum of $a\text{TiO}_2$, along with the FMS-computed $k^2\chi(k)_{\text{MD}}$ function from MD-structural trajectories of $a\text{TiO}_2$. Just for the sake of spectral-shape comparison, the $k^2\chi(k)$ spectrum of anatase TiO_2 is also shown [Fig. 1(b); fitted by ARTEMIS]. When going from crystalline to $a\text{TiO}_2$, structural disorder around photoabsorbing Ti atoms reduces the oscillation amplitude in $k^2\chi(k)$

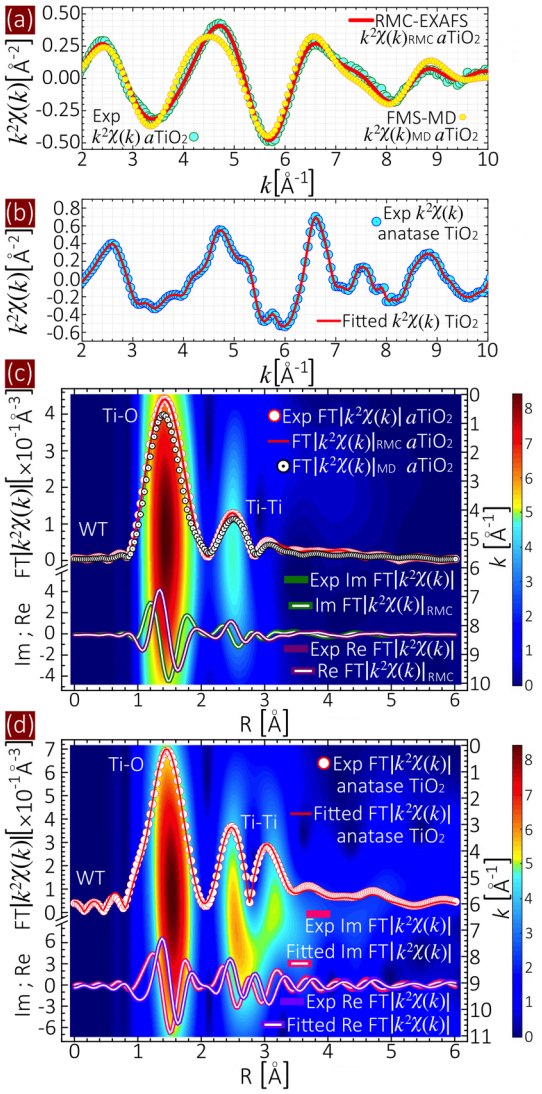

FIG. 1. (a) Experimental $k^2\chi(k)$ spectrum of aTiO$_2$ (circles, phase uncorrected), fitting from RMC-EXAFS simulations $k^2\chi(k)_{RMC}$ (line), and FMS-MD computed $k^2\chi(k)_{MD}$ function (dots). (b) Experimental $k^2\chi(k)$ spectrum of anatase TiO$_2$ (circles), and nonlinear least-squares fitting by single and multiple scattering by ARTEMIS (line). (c) Background: WT of $k^2\chi(k)$ for aTiO$_2$. Top: FT$|k^2\chi(k)|$ [circles], RMC-EXAFS simulated FT$|k^2\chi(k)|_{RMC}$ [line], and FMS-MD computed FT$|k^2\chi(k)|_{MD}$ function [black circles]. Bottom: Real and Im parts of FT$|k^2\chi(k)|$. (d) Background: WT of $k^2\chi(k)$ for anatase TiO$_2$. Top: FT$|k^2\chi(k)|$ [circles], and least-squares fitting by single and multiple scattering by ARTEMIS [line]. Bottom: Real and Im parts of FT$|k^2\chi(k)|$ for anatase TiO$_2$.

at high k values. The RMC-EXAFS simulated $k^2\chi(k)_{RMC}$ spectrum is in good agreement with experimental data. After convergence, a minimum residual of $\sim$1–5 $\times$ 10^{-3} is attained, which shows that RMC-EXAFS simulations properly reflect the disordered structure of aTiO$_2$. The FMS-MD simulated $k^2\chi(k)_{MD}$ function properly reproduces the phase, shape, and damping of oscillations in the experimental $k^2\chi(k)$ spectrum. The corresponding wavelet transforms [WT] of $k^2\chi(k)$ spectra are displayed in Figs. 1(c) and 1(d) [two-dimensional contour plots]. The WT of $k^2\chi(k)$ for aTiO$_2$ shows two intensities at

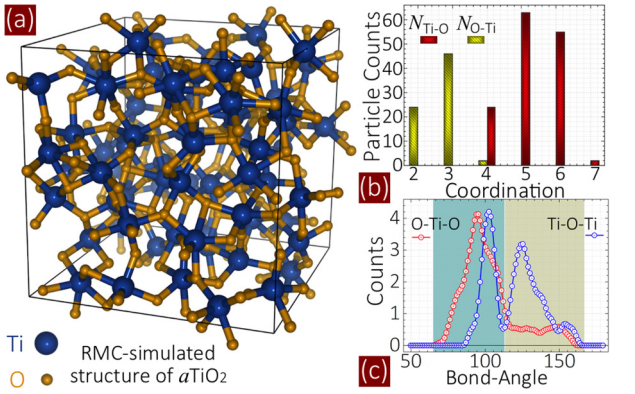

FIG. 2. (a) The RMC-EXAFS simulated structure of aTiO$_2$. (b) Distribution of local coordination at the Ti and O shells. (c) The O–Ti–O and Ti–O–Ti bond-angle distributions.

R $\approx$ 1.45 Å [$k \approx$ 5.2 Å^{-1}] and R $\approx$ 2.52 Å [$k \approx$ 5.8 Å^{-1}], associated to backscattering by neighboring O and Ti atoms at the first and second coordination shells of the photoabsorbing Ti atoms. Absence of higher coordination shells in aTiO$_2$ when comparing with anatase TiO$_2$ [shells at R $\approx$ 1.45; R $\approx$ 2.48; R $\approx$ 3.04 Å] is due to the loss of long-range order. The RMC-EXAFS refinement, FT$|k^2\chi(k)|_{RMC}$, of the experimental Ti–O and Ti-Ti coordination shells in the Fourier transformed FT$|k^2\chi(k)|$ for aTiO$_2$, is displayed on top of WT in Fig. 1(c) [phase uncorrected]. FMS-MD computed FT$|k^2\chi(k)|_{MD}$ from the $k^2\chi(k)_{MD}$ function is also displayed. For the sake of spectral-shape comparisons, fitting of FT$|k^2\chi(k)|$ of anatase TiO$_2$ is shown on top of WT in Fig. 1(d) [fitted by ARTEMIS]. The RMC-EXAFS, FT$|k^2\chi(k)|_{RMC}$, and FMS-MD, FT$|k^2\chi(k)|_{MD}$, simulated functions reproduce the real-space position of the Ti–O and Ti-Ti coordination shells of the experimental spectrum. The close similarity between $k^2\chi(k)_{RMC}$, FT$|k^2\chi(k)|_{RMC}$ and $k^2\chi(k)_{MD}$, and FT$|k^2\chi(k)|_{MD}$ functions evidences that the atomic short-range order of aTiO$_2$ can be properly reproduced by RMC-EXAFS and FMS-MD-EXAFS simulations based on *ab initio* approaches. The remaining small differences between the experimental spectra and FMS-MD computed $k^2\chi(k)_{MD}$ and FT$|k^2\chi(k)|_{MD}$ functions could possibly be ascribed to the size of the simulation cell and approximations on the muffin-tin radii for the potential of the photoabsorbing Ti atoms [38].

To more quantitatively describe the atomic short-range structural order in aTiO$_2$ we analyze the local bonding and coordination around Ti and O atoms. RMC-EXAFS simulated structures of aTiO$_2$ exhibit edge- and corner-sharing distorted TiO$_x$ units [Fig. 2(a)]. Distribution at the Ti and O coordination shells [see Fig. 2(b)] indicates that the Ti atoms hold mainly undercoordinated TiO$_4$ tetrahedra [N_{Ti} = 4; 17%], TiO$_6$ octahedra [N_{Ti} = 6; 38%], and TiO$_5$ pentahedra [N_{Ti} = 5; 44%]. Overcoordinated TiO$_7$-octahedra [N_{Ti} = 7] unit blocks also exist, but contribute merely 1%. Realization of TiO$_7$ units was also observed in MD simulations, and they could in principle compensate for the occurrence of a large amount of undercoordinated TiO$_4$ units [19]. The O atoms hold mainly threefold coordination with Ti atoms [N_O = 3; 64%]; undercoordinated twofold [N_O = 2; 33%] and overcoordinated

TABLE I. Main interatomic distances, coordinations, and $2\sigma^2$ of aTiO$_2$ and anatase TiO$_2$ obtained from $k^2\chi(k)$; FT$|k^2\chi(k)|$ spectral-fitting by ARTEMIS, and parameters calculated from RMC-EXAFS and *ab initio* FMS-MD simulations of aTiO$_2$.

Least-squares fitting[a]			Simulated aTiO$_2$		
	TiO$_2$	aTiO$_2$	RMC-EXAFS[b]		MD[c]
	First shell	First shell	O-O	2.6(7) Å	2.6(9) Å
Ti–O	1.9(5) Å	1.9(6) Å	Ti–O	1.9(6) Å	1.9(6) Å
$N_{\text{Ti–O}}$	6.0	5.4(2)	$N_{\text{Ti–O}}$	5.2(4)	5.5(9)
$2\sigma^2_{\text{Ti–O}}$	0.011(8)	0.018(4)	$N_{\text{O-Ti}}$	2.6(8)	2.8(2)
	Second shell	Second shell	$N_{\text{O-O}}$	8.9(8)	9.6(3)
Ti-Ti	3.0(4) Å	3.1(2) Å	Ti-Ti	3.1(8) Å	3.1(5) Å
$N_{\text{Ti-Ti}}$	4.0	2.7(4)		3.5(4) Å	3.5(2) Å
$2\sigma^2_{\text{Ti-Ti}}$	0.012(2)	0.026(2)	$N_{\text{Ti-Ti}}$	2.6(8)	2.8(8)

[a]Refined by ARTEMIS: $S_0^2 \approx 0.90(2)$; $\Delta E_0 \approx -4.87$ eV.
[b]RMC-EXAFS simulations: $S_0^2 \approx 0.94(2)$ eV.
[c]FMS calculated from MD simulations: $S_0^2 \approx 0.88(4)$ eV.

fourfold [$N_{\text{O}} = 4$; 3%] units also occur. O–Ti–O bond-angle distribution exhibits two maxima at $\Theta = 94°$–$104°$ associated to the main bond angles between a Ti atom and two edge-sharing O atoms. Ti–O–Ti bond-angle distribution displays maxima at $\Theta = 102$–$125°$ due to the bond angles between O and two corner-sharing Ti atoms [Fig. 2(c)]. We note that all the RMC-EXAFS refined structures of aTiO$_2$ display similar atomic bonding, coordinations, and bond-angle distributions. This is in part induced by the structural constraints applied in simulations, which force the input structures to attain analogous structural order, and thus similar contributions to the EXAFS signal. In fact, as we will show in Sec. IV B, distributions of TiO$_{5;6}$ units consistently obtained for all RMC-EXAFS refined structures of aTiO$_2$ yield A$_2$ pre-edge-XANES spectra, the relative intensity, energy position, and weight of which rightly reproduce the measured spectra. Some structures do not hold TiO$_7$ units, but instead they reach a major number of TiO$_{5;6}$ units. Structures having higher undercoordinated TiO$_4$ units exhibit an intense A$_1$ pre-edge-XANES peak, and thus they are unrealistic because of their inability to reproduce simultaneously the EXAFS and XANES spectra. No inclusion of bonding constraints results in structures having short Ti–O bonds, which also induces high intensity pre-edge XANES spectra. From those results it is concluded that RMC-EXAFS simulated structures with proportional distribution of TiO$_{5;6}$ units and main interatomic bond distance Ti–O $\approx 1.9(6)$ Å dominate accurately the structural characteristics of the final EXAFS and XANES spectra of our aTiO$_2$ thin-film oxides.

Total and partial PDFs, $g(\mathbf{r})$'s, for RMC-EXAFS and MD-simulated structures of aTiO$_2$ are displayed in Figs. 3(a)–3(d). For comparison, $g(\mathbf{r})$'s of anatase TiO$_2$ are also shown. The $g(\mathbf{r})$'s display sharp peaks between $\mathbf{r} \approx 1.6$ and 4.0 Å; beyond that range the $g(\mathbf{r})$'s are damped out due to structural disorder. Local coordination is lower in RMC-EXAFS than in MD-simulated structures of aTiO$_2$, but both are lower than that of anatase TiO$_2$ [Figs. 3(e)–3(h)]. Data in Table I show an excellent agreement between the main interatomic distances and atomic coordinations obtained from

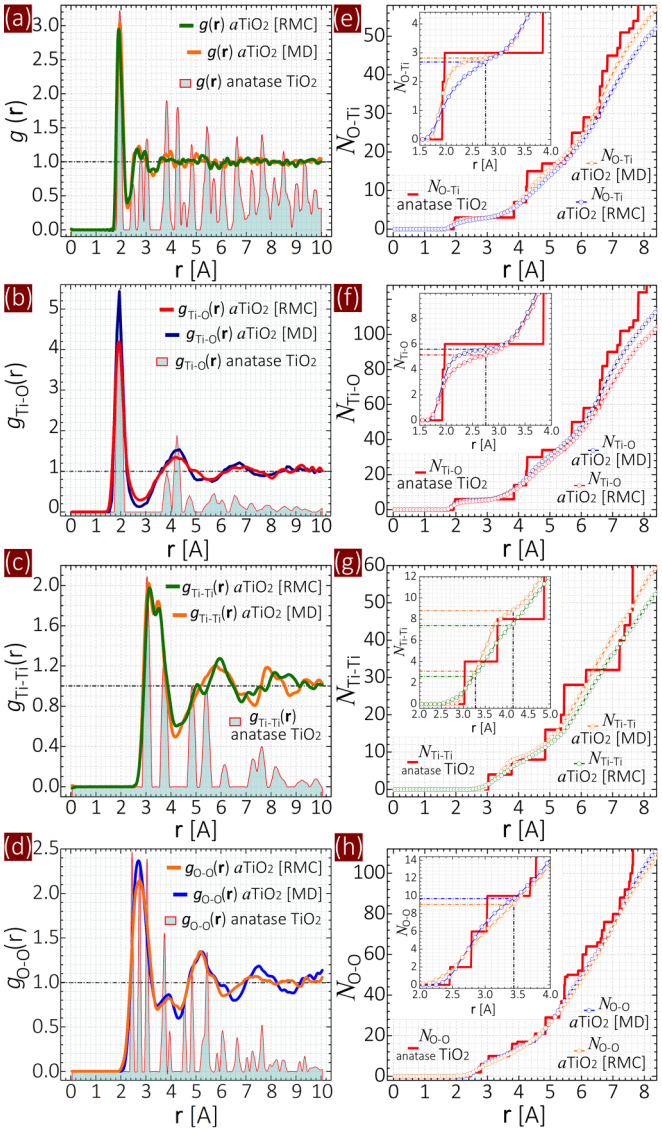

FIG. 3. (a)–(d) Total and partial $g(\mathbf{r})$'s of RMC-EXAFS and MD simulated structures of aTiO$_2$ [lines], and anatase TiO$_2$ [peaks]. (e)–(h) Coordination N for aTiO$_2$ [circles] from RMC-EXAFS and MD simulated structures of aTiO$_2$, and anatase TiO$_2$ [line]. Insets show a zoom of the first coordination shells.

nonlinear least-squares fitting of the experimental $k^2\chi(k)$ and FT$|k^2\chi(k)|$ spectra, and those calculated from RMC-EXAFS and MD simulation of aTiO$_2$. Debye-Waller factors σ^2 reflect the attenuation of $k^2\chi(k)$ due to the mean-square static disorder in the distribution of interatomic bond distances and atomic displacements [27]. Thus, increases in σ^2 factors give a measure of the degree of disorder in aTiO$_2$, which is manifested in lowering local coordinations and increasing the Ti–O, Ti–Ti, and O–O interatomic distances in aTiO$_2$. Results in Table I are in agreement with EXAFS data reported for sputtered and ion-beam deposited aTiO$_2$ films [39,40]. Early studies of electron and x-ray diffraction reported similar structural parameters, and from RMC-PDF fitting it was stated that sputtered aTiO$_2$ films resemble a brookite phase [13]. However, a similar RMC-PDF scheme applied to aTiO$_2$ nanoparticles prepared by hydrolysis state that such systems hold a distorted shell

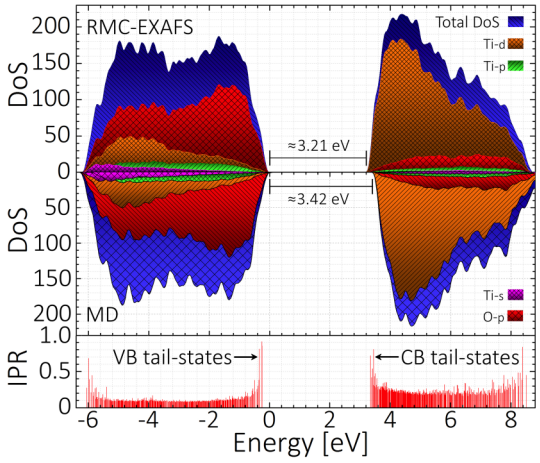

FIG. 4. Density of states [DoS] displaying the O-p, and Ti-$[s,p,d]$ character of the VB and CB for RMC-EXAFS [top], and MD [middle] simulated structures of $a\text{TiO}_2$. Bottom: the IPR showing the localization of the VB- and CB-tail states.

surrounding a crystalline anatase core [15]. Although results differ among simulated systems, it should be noted that different deposition conditions yield variations in the ratio of edge to vertex linked octahedral building units, which influences the short-range order in various $a\text{TiO}_2$ systems [41]. Our experimental EXAFS data, RMC-EXAFS, and MD simulations of $a\text{TiO}_2$ do not suggest the existence of a single local order. Instead, the wide distribution of interatomic distances and ratio of edge- to corner-sharing distorted TiO_x units suggest the mixture of the symmetries and coordinations present in the different polymorphs and Magnéli phases [M-P] of TiO_2. In fact, M-P consists of undercoordinated $\text{TiO}_{4,5}$ units. TiO_7 units occur in monoclinic TiO_2-baddeleyite-$P2_1/c$, and orthorhombic TiO_2-Pbca polymorphs [42–44]. A large amount of $\text{TiO}_{5,6}$ units would also explain why the amorphous phase transforms into either anatase or rutile rather than to a brookite phase upon heating [14]. This is also supported by neutron diffraction and XAS studies, which suggest that $a\text{TiO}_2$ systems involve the mixture between crystalline domains with several TiO_2 phases and undercoordinated TiO_x units [16]. Difficulties with RMC-PDF schemes arise from the possibility for multiple atomic configurations to have the same PDF. This is due to the inability of RMC-PDF schemes to recover the right statistic of two- and three-body correlations in the nearest atomic-coordination shells [17]. Here, self-consistent calculations of the cluster potential considering single and multiple scattering were applied to obtain preconverged scattering amplitudes and phase shifts for each photoabsorbing Ti atom which removes some of these difficulties. The RMC-EXAFS simulations were implemented while the structure was optimized after each atomic movement. Thus, since structural parameters were calculated at each cycle, we expect our RMC-EXAFS-based simulations to properly resemble the disordered structure of $a\text{TiO}_2$.

B. Electronic properties of $a\text{TiO}_2$ by XANES-DFT

The projected density of states [DoS] of RMC-EXAFS and MD-simulated structures of $a\text{TiO}_2$ are displayed in Fig. 4. The DoS shows that in $a\text{TiO}_2$ the VB comprises mostly O-$[2p]$ states, while the CB consists mainly of Ti-$[3d]$-like states. For RMC-EXAFS simulated structures of $a\text{TiO}_2$ the DoS unveils a band gap of ≈3.21 eV, without state defects yielding in-gap states. MD-generated structures of $a\text{TiO}_2$ exhibit similar DoS, with a comparable energy band gap of ≈3.42 eV. High intensity observed in the inverse participation ratio [IPR], at the VB and CB edges, suggests electronic localization of the O-$[2p]$ VB- and Ti-$[3d]$ CB-tail states [bottom Fig. 4]. The degree of localization of the VB and CB tail states depends on the charge-density contributions arising from the short-range order of under and overcoordinated TiO_x and Ti_xO units. Using our consistent scheme generating representative amorphous structures from experimental data, our calculated energy band gap is 0.48 eV lower than previous values obtained for $a\text{TiO}_2$ using the HSE06 functional [19], and is in good agreement with the experimental optical band gap $\hbar\omega_g \approx 3.28 \pm 0.07$ eV, previously reported for $a\text{TiO}_2$ thin-film oxides by UV-vis-NIR spectroscopy [4].

Figure 5(a) displays experimental and FDM-computed Ti K-edge RMC-XANES and MD-XANES spectra of $a\text{TiO}_2$. Experimental spectra are in good agreement with data reported for sputtered and ion-beam deposited $a\text{TiO}_2$ films [39,40]. The FDM-RMC-XANES and FDM-MD-XANES functions properly reproduce all features, including position and relative intensity of the pre-edge structure [that is, peak A_2] in the measured XANES spectrum of $a\text{TiO}_2$. This finding further validates that the simulated RMC-EXAFS atomic short-range order and especially atomic coordination around photoabsorbing Ti atoms properly reflects those in the disordered structure of $a\text{TiO}_2$. This is because relative position and intensity of the pre-edge peak A_2 are highly sensitive to distributions of interatomic bond distances, bond angles, and coordinations [26]. For the sake of comparison, note that all characteristics and pre-edge structure [peaks A_1; A_2; A_3] of the measured XANES spectrum of anatase TiO_2 are well produced by its computed FDM-XANES function [Fig. 5(b)]. Interestingly, the pre-edge structure in the XANES spectra of $a\text{TiO}_2$ unveils an enhanced absorption peak at $A_2 \approx 4970.8$ eV [Fig. 5(a)]. This differs from the triple-peak structure because of the TiO_6-octahedron crystal-field splitting found in anatase TiO_2 [peaks $A_1 \approx 4968.7$; $A_2 \approx 4971.9$; $A_3 \approx 4974.2$ eV in Fig. 5(b)]. However, the strongly distorted TiO_x units, with out-of-center distortion of Ti atoms and deviation in O–Ti–O and Ti–O–Ti bond lengths and bond angles in $a\text{TiO}_2$, remove degenerated states and reduce the magnitude of the crystal-field splitting. Thus, the local disorder around photoabsorbing Ti atoms at the first and second coordination shells induces strong Ti^{4+}-$[p$-$d]$ orbital mixing yielding the intense pre-edge structure A_2 characteristic of the XANES spectra of $a\text{TiO}_2$.

The CB states of the Ti projected DoS, which maps the Ti K-edge XANES spectrum of $a\text{TiO}_2$, show that the pre-edge region [4964.1–4974.8 eV XANES → 2.8–10.0 eV DoS] comprises mainly d states, with lower contributions from p and s states [bottom and inset 1 in Fig. 5(a)]. However, because of the sharp DoS of the Ti d states the quadrupole Ti $[1s \rightarrow d]$ transitions are negligible compared to dipole Ti $[1s \rightarrow p]$ transitions. The [Ti-s,p,d] orbitals are not degenerated, exhibiting a dispersive character due to the local disorder around Ti and O atoms; then their contributions to the local DoS have the same character. Thus, the symmetry of the

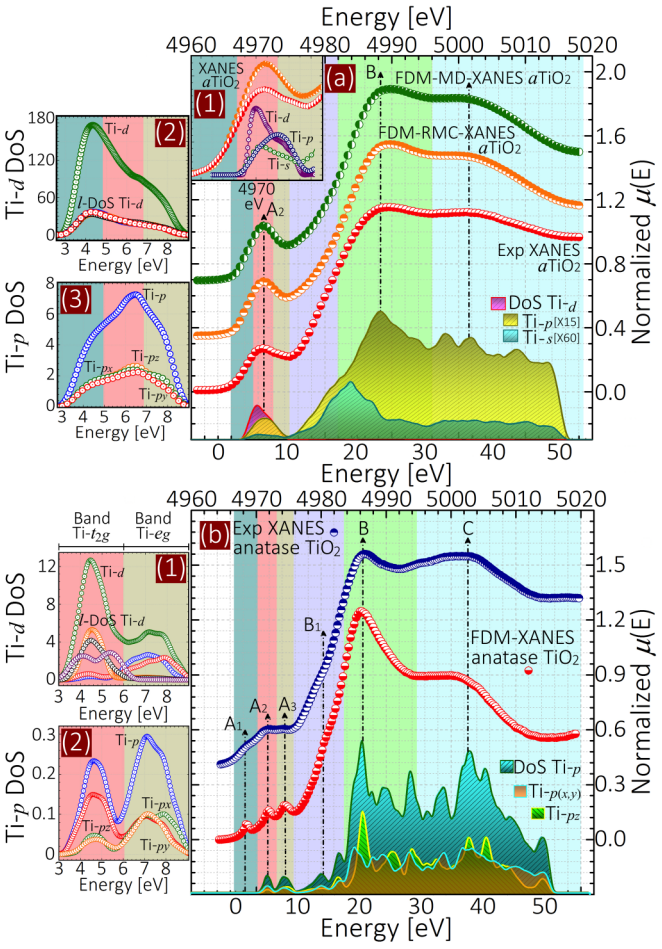

FIG. 5. (a) Experimental and FDM-computed Ti K-edge XANES spectra of aTiO$_2$ [half circles], which follow the distribution of Ti-[s,p,d] DoS [at bottom]. Insets 1–3 zoom the pre-edge structure, and Ti-[s,p,d] DoS giving rise to the pre-edge peak A$_2$ of XANES spectra in aTiO$_2$. (b) Experimental and FDM-computed XANES spectra of anatase TiO$_2$, following the [Ti-p] DoS. Insets 1 and 2 show crystal-field splitting of [Ti-p,d] states into [Ti-t_{2g}; e_g] bands giving rise to the pre-edge peaks A$_2$; A$_3$ of XANES spectra in TiO$_2$. XANES spectra are displaced vertically for clarity. Note: For accurate description of the whole XANES spectral range in terms of DoS, the [Ti-$s,p_{[x,y,z]},d$] l-DoS shown at bottom of Figs. 5(a) and 5(b) were calculated in the all-electron full-potential linearized augmented plane-wave [FP-LAPW] method given in Ref. [45].

[Ti-s,p,d] orbital mixing has a strong character [insets 2 and 3 in Fig. 5(a)]. This means that the electronic dipole hybridized [Ti-t_{2g}] [$1s \rightarrow 4p$-$3d$] and [Ti-e_g] [$1s \rightarrow 4p$-$3d$] transitions on the neighboring Ti atoms at the second coordination shell become strongly allowed. Those [Ti-t_{2g}] and [Ti-e_g] electronic transitions merge into a single intense absorption peak, which comprises the pre-edge structure at A$_2 \approx 4970.8$ eV, in the Ti K-edge XANES spectra of aTiO$_2$. Beyond ≈4974.8 eV, p-d orbital mixing is responsible for the absorption intensity in the XANES spectra. The *white line* at B ≈ 4988.8 eV could be ascribed to higher-lying p atomic orbitals. Note that all the peaks in the experimental XANES and FDM-RMC-XANES and FDM-MD-XANES spectra are well reproduced by the calculations and can be assigned to main peaks in the projected Ti-p DoS of the CB states.

Note that in anatase TiO$_2$ the crystal field splits Ti-[$3d$] states into t_{2g} [$d_{xy}; d_{xz}; d_{yz}$] and e_g [$d_{x^2-y^2}; d_{z^2}$] orbitals, which give rise to the pre-edge peaks A$_2 \approx 4971.9$ eV and A$_3 \approx$ 4974.2 eV [insets 1 and 2 in Fig. 5(b)]. The pre-edge peak A$_1 \approx$ 4968.7 eV due to quadrupole [Ti-t_{2g}] [$1s \rightarrow 3d$] transitions is a band hybridization effect, which mixes p states into d bands giving a dipole allowed transition [46].

Finally, in order to assess the influence of disorder in the crystal-field splitting of aTiO$_2$, the O K-edge XANES spectrum of aTiO$_2$ was computed by FDM simulations of its RMC-EXAFS generated structure [see Fig. 6]. The spectrum exhibits two peaks associated to the transitions from the O-[$1s$] core level into the t_{2g} and e_g bands due to hybridization of unoccupied O-[p] states with unoccupied [Ti-s,p,d] orbitals, which are clearly resolved in the O-[s,p] projected DoS. A broad feature between ∼535.5 and 556 eV due to O-[p] states hybridized with [Ti-s,p] states is also well resolved. The e_g band exhibits lower intensity with respect to the t_{2g} band. This increase in the t_{2g}/e_g intensity ratio is because of a weaker crystal-field interaction caused by the distorted symmetry of undercoordinated Ti [$N_{\text{Ti–O}} = 5.24$] and O atoms [$N_{\text{O-Ti}} = 2.68$]. This fact is supported by previous experimental results reported for thermally grown aTiO$_{2-x}$ layers, where the e_g band exhibits lower intensity when comparing with anatase TiO$_2$ [7]. From the relative energy position of the t_{2g} and e_g bands in the O K-edge XANES spectrum, the crystal-field splitting of aTiO$_2$ is $\Delta d \approx E(e_g)$-$E(t_{2g}) \approx 2.4 \pm 0.3$ eV, which is lower than in anatase TiO$_2$ [$\Delta d \approx 2.9$ eV [47]]. Considering that [Ti-e_g] orbitals point toward neighboring O-[p] orbitals, then the low crystal-field splitting can be ascribed to short-range disorder at the first and second coordination shells around Ti and O atoms in aTiO$_2$.

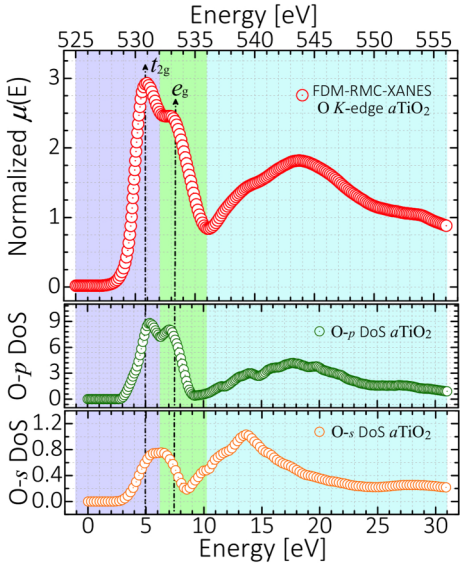

FIG. 6. O K-edge FDM-XANES spectrum of aTiO$_2$ calculated from its RMC-EXAFS simulated structure [top], and O-[s,p] DoS [bottom] [crystal-field splitting $\Delta d \approx 2.4 \pm 0.3$ eV].

V. CONCLUSIONS

We have properly simulated the short-range structural order of $a\text{TiO}_2$ from modeling of the experimental XAS spectra by RMC-EXAFS and FMS-MD simulations. The proper reproduction of the relative intensity and weight of the pre-edge structure of the XANES spectra prove that the amount of undercoordinated TiO_x units closely resembles the coordination of the experimental data. Electronic hybridization of the central Ti-p orbitals with the Ti-d orbitals is strongly dependent on the second Ti coordination shell. The character of ligands and neighboring atoms around Ti sites affects the energy splitting of the electronic levels at the Ti-[p-d] manifolds. The experimental XAS spectra and in particular the pre-edge structure of the XANES spectra of $a\text{TiO}_2$ is consistent with the projected DoS on the photoabsorbing Ti atoms. From structural analysis, it was found that proper reproduction of the local-structural order and XAS spectra requires us to take into account the influence of atoms beyond the first coordination shell. Several studies have simulated XAS spectra of amorphous systems from structurally distorted small clusters [stretching and shortening of bond lengths or tilting and twisting of bond angles]. However, our calculations of XANES-pre-edge spectra suggest that such approximations are not reliable because distorted clusters do not hold the lowest energy state, and are structurally unrealistic when comparing with experimental data. Our approach provides a systematic method to extract the atomic short-range structural order of amorphous systems, from which electronic properties can be analyzed in terms of the projected DoS and experimental XANES data. The approach presented here provides a consistent route to experimentally/theoretically analyze how local disorder affects the electronic properties in $a\text{TiO}_2$, and could be potentially applied to other disordered systems. Further studies are being conducted in order to describe how introduction of oxygen vacancies in $a\text{TiO}_{2-x}$ induces Fermi-level rises, band-gap widening, d-orbital filling, and optical absorption. Local-structural distortions are linked to Ti^{3+} polaronic states in the lower part of the CB, arising from transfer of electrons from oxygen vacancies, and hopping upon photon absorption and thermal excitation will be reported in future studies of $a\text{TiO}_{2-x}$ systems.

ACKNOWLEDGMENTS

This work has been supported by the Swedish Research Council. Computational facilities were provided by the Swedish National Infrastructure for Computing (SNIC) at PDC Center for High Performance Computing and National Supercomputer Center at Linköping University (triolith). Portions of this research were carried out at Beamline I811, MAX-Lab Synchrotron Radiation Source, Lund University, Sweden. Funding for the Beamline I811 project was kindly provided by The Swedish Research Council and The Knut och Alice Wallenbergs Stiftelse.

[1] J. Shi, Z. Li, A. Kvit, S. Krylyuk, A. V. Davydov, and X. Wang, Nano Lett. **13**, 5727 (2013).
[2] H. Xiong, M. D. Slater, M. Balasubramanian, C. S. Johnson, and T. Rajh, J. Phys. Chem. Lett. **2**, 2560 (2011).
[3] Y.-M. Lin, P. R. Abel, D. W. Flaherty, J. Wu, K. J. Stevenson, A. Heller, and C. B. Mullins, J. Phys. Chem. C **115**, 2585 (2011).
[4] C. A. Triana, C. G. Granqvist, and G. A. Niklasson, J. Appl. Phys. **119**, 015701 (2016).
[5] C. A. Triana, C. G. Granqvist, and G. A. Niklasson, J. Phys: Conf. Series **559**, 012004 (2014).
[6] D. H. Kwon, K. M. Kim, J. H. Jang, J. M. Jeon, M. H. Lee, G. H. Kim, X. S. Li, G. S. Park, B. Lee, S. Han, M. Kim, and C. S. Hwang, Nat. Nanotechnol. **5**, 148 (2010).
[7] K.-H. Choi, K.-B. Chung, and H.-K. Kim, Appl. Phys. Lett. **102**, 153511 (2013).
[8] S. Hu, M. R. Shaner, J. A. Beardslee, M. Lichterman, B. S. Brunschwig, and N. S. Lewis, Science **344**, 1005 (2014).
[9] P. W. Anderson, Phys. Rev. Lett. **34**, 953 (1975).
[10] N. Mott, Rev. Mod. Phys. **50**, 203 (1978).
[11] M. H. Cohen, H. Fritzsche, and S. R. Ovshinsky, Phys. Rev. Lett. **22**, 1065 (1969).
[12] X. Chen, Science **331**, 746 (2011).
[13] V. Petkov, G. Holzhuter, U. Troge, Th. Gerver, and B. Himmel, J. Non-Cryst. Solids **231**, 17 (1998).
[14] H. Zhang and J. F. Bandfiel, Chem. Mater. **14**, 4145 (2002).
[15] H. Zhang, B. Chen, J. F. Banfield, and G. A. Waychunas, Phys. Rev. B **78**, 214106 (2008).
[16] W. J. H. Borghols, D. Lutzenkirchen-Hecht, U. Haake, W. Chan, U. Lafont, E. M. Kelder, E. R. H. van Eck, A. P. M. Kentgens, F. M. Mulder, and M. Wagemaker, J. Electrochem. Soc. **157**, A582 (2010).
[17] K. Nemeth, K. W. Chapman, M. Balasubramanian, B. Shyam, P. J. Chupas, S. M. Heald, M. Newville, R. J. Klingler, R. E. Winans, J. D. Almer, G. Sandi, and G. Srajer, J. Chem. Phys. **136**, 074105 (2012).
[18] K. K. Ghuman and C. V. Singh, J. Phys.: Condens. Matter **25**, 475501 (2013).
[19] M. Landmann, T. Kohler, S. Koppen, E. Rauls, T. Frauenheim, and W. G. Schmidt, Phys. Rev. B **86**, 064201 (2012).
[20] V. Krayzman, I. Levin, J. Woicik, T. Proffen, T. Vanderah, and M. Tucker, J. Appl. Crystallogr. **42**, 867 (2009).
[21] C. Massobrio, J. Du, M. Bernasconi, and P. S. Salmon, *Molecular Dynamics Simulations of Disordered Materials* (Springer, Switzerland, 2015), Vol. 215, p. 181.
[22] H. Yoshitake, T. Sugiharab, and T. Tatsumi, Phys. Chem. Chem. Phys. **5**, 767 (2003).
[23] G. Mountjoy, D. M. Pickup, G. W. Wallidge, R. Anderson, J. M. Cole, R. J. Newport, and M. E. Smith, Chem. Mater. **11**, 1253 (1999).
[24] F. Farges, G. E. Brown, and J. J. Rehr, Phys. Rev. B **56**, 1809 (1997).
[25] G. Mountjoy, D. M. Pickup, R. J. Newport, and M. E. Smith, J. Phys. Chem. B **105**, 6273 (2001).
[26] N. Jiang, D. Su, and J. C. H. Spence, Phys. Rev. B **76**, 214117 (2007).

[27] A. L. Ankudinov, B. Ravel, J. J. Rehr, and S. D. Conradson, Phys. Rev. B **58**, 7565 (1998).
[28] O. Bunau and Y. Joly, J. Phys.: Condens. Matter **21**, 345501 (2009).
[29] G. Kresse and J. Furthmuller, Phys. Rev. B **54**, 11169 (1996).
[30] S. Carlson, M. Clausen, L. Gridneva, B. Sommarin, and C. Svensson, J. Synchrotron Radiat. **13**, 359 (2006).
[31] B. Ravel and M. Newville, J. Synchrotron Radiat. **12**, 537 (2005).
[32] M. G. Tucker, D. A. Keen, M. T. Dove, A. L. Goodwin, and Q. Hui, J. Phys.: Condens. Matter **19**, 335218 (2007).
[33] W. Kohn and L. J. Sham, Phys. Rev. **140**, A1133 (1965).
[34] J. P. Perdew, K. Burke, and M. Ernzerhof, Phys. Rev. Lett. **77**, 3865 (1996).
[35] P. E. Blöchl, Phys. Rev. B **50**, 17953 (1994).
[36] H. J. Monkhorst and J. D. Pack, Phys. Rev. B **13**, 5188 (1976).
[37] J. Paier, M. Marsman, K. Hummer, G. Kresse, I. C. Gerber, and J. G. Ángyán, J. Chem. Phys. **124**, 154709 (2006).
[38] B. J. Palmer, D. M. Pfund, and J. L. Fulton, J. Phys. Chem. **100**, 13393 (1996).
[39] A. Caballero, D. Leinen, A. Fernández, A. Justo, J. P. Espinós, and A. R. González-Elipe, J. Appl. Phys. **77**, 591 (1995).
[40] D. Carta, G. Mountjoy, A. Regoutz, A. Khiat, A. Serb, and T. Prodromakis, J. Phys. Chem. C **119**, 4362 (2015).
[41] E. G. Seebauer and M. C. Kratzer, *Charged Semiconductor Defects* (Springer-Verlag, London, 2009), p. 268.
[42] L. Liborio, G. Mallia, and N. Harrison, Phys. Rev. B **79**, 245133 (2009).
[43] H. Sato, S. Endo, M. Sugiyama, T. Kikegawa, O. Shimomura, and K. Kusaba, Science **251**, 786 (1991).
[44] N. A. Dubrovinskaia, L. S Dubrovinsky, R. Ahuja, V. B. Prokopenko, V. Dmitriev, H. P. Weber, J. M. Osorio-Guillen, and B. Johansson, Phys. Rev. Lett. **87**, 275501 (2001).
[45] All-electron full-potential linearized augmented plane-wave [FP-LAPW] DFT calculations were implemented in the ELK code [http://elk.sourceforge.net]. The Perdew-Burke-Ernzerhof generalized gradient approximation [PBE-GGA] was applied. The wave functions inside the muffin tins were expanded up to $l_{\max} = 8$ and the plane waves were expanded with a cutoff of $\mathbf{R}_{\min}^{\mathrm{MT}} \times \mathbf{K}_{\max} = 8.5$ [$\mathbf{R}_{\min}^{\mathrm{MT}}$: Smallest muffin-tin radius; $\mathbf{K}_{\max} = |\mathbf{G}+\mathbf{k}|$: Maximum value of the wave vector]. The muffin-tin radii were chosen as $\mathbf{R}_{\mathrm{Ti}}^{\mathrm{MT}} = 1.27$ Å, and $\mathbf{R}_{\mathrm{O}}^{\mathrm{MT}} = 0.95$ Å. k meshes of $1 \times 1 \times 1$ [$a\mathrm{TiO_2}$], and $10 \times 10 \times 10$ [anatase $\mathrm{TiO_2}$] were used.
[46] Y. Joly, D. Cabaret, H. Renevier, and C. R. Natoli, Phys. Rev. Lett. **82**, 2398 (1999).
[47] F. M. F. de Groot, J. Faber, J. J. M. Michiels, M. T. Czyżyk, M. Abbate, and J. C. Fuggle, Phys. Rev. B **48**, 2074 (1993).